

Testing of telescope optics: a new approach

C. Roddier, F. Roddier, A. Stockton, A. Pickles

Institute for Astronomy, University of Hawaii

N. Roddier

Department of Electrical Engineering, University of Arizona

ABSTRACT

Curvature sensing has been proposed recently as a possible substitute for slope sensing to reconstruct optical wavefronts. Hartmann slope sensors are currently used to test telescope optics under operating conditions. This paper describes recent results obtained with the curvature-sensing approach. The method consists of taking long-exposure CCD images of the beam cross-section on each side of the telescope focal plane. A program based on the solution to the Poisson equation is used to reconstruct the wavefront.

Compared with current Hartmann sensing techniques, this method has the following advantages:

1. The sensitivity is comparable to that of the Shack-Hartmann test.
2. No extra optics are necessary, resulting in a better throughput.
3. No calibration with a reference plane wave is required.

Data have been taken at the prime focus of the University of Hawaii 88-inch Ritchey-Chrétien telescope. Rather than using a null lens, we have computationally removed the spherical aberration produced by the hyperbolic primary. A map of the residual wavefront errors has been obtained as a solution of the Poisson equation.

1. INTRODUCTION

The observation of out-of-focus stellar images has long been known as a sensitive test for mirror figure errors. It has sometimes been referred to as the eyepiece test or the inside-and-outside test and was apparently often rediscovered. Surprisingly, there has been very little directed toward extracting quantitative information from such observations. A. Behr¹ and later E. Ruiz *et al.*² described the effect of coma on out-of-focus images and proposed the test as a means to align telescope optics. Beckers and Williams³ described out-of-focus images recorded at the MMT and correctly interpreted the observed zones as local curvature errors on the wavefront. Only recently, one of us⁴ proposed a general method to reconstruct wavefronts from out-of-focus images. The performance of the method has been analysed and the results of laboratory experiments have been presented⁵. The method is briefly described in §2. Experimental data obtained at the UH 88-inch telescope are presented in §3. A detailed description of their analysis is given in the following sections. Results are summarized in the last section.

2. DESCRIPTION OF THE METHOD

Basically, the method consists of measuring both the illumination $I_1(\vec{r})$ in a plane P_1 at a distance l before the telescope focal plane F and the illumination $I_2(-\vec{r})$ in plane P_2 symmetrically at the same distance l beyond F (Fig. 1). Theoretically, to insure symmetry, a lens L_2 with focal length $f/2$ equal to half the focal length f of the telescope should be used in plane F to reimage the telescope objective L_1 at a distance f beyond F . In practice, since l is very small compared to f , L_2 can be easily left out. A local wavefront curvature error makes the light converge closer to one plane than the other, producing an excess of illumination in this plane and a lack of illumination in the other plane. The difference $\Delta I = I_1(\vec{r}) - I_2(-\vec{r})$ between the two illuminations provides a measure of the local wavefront curvature or Laplacian of the wavefront surface.

According to geometrical optics, assuming $l \ll f$,

$$\frac{\Delta I}{I}(\vec{r}) = 2 \frac{\lambda f^2}{l R^2} \nabla^2 Z(\vec{r}) \quad (1)$$

where $I = (I_1 + I_2)/2$ is the average illumination, \vec{r} is a position vector on the telescope pupil expressed in pupil radius

units, R is the pupil radius, and Z is the wavefront surface in wavelength λ units. The result is fairly insensitive to nonuniformities of the light distribution in the pupil plane, since they produce a similar excess or lack of illumination in both planes that cancels out when taking the normalized difference. Radial wavefront tilts at the pupil edge produces local shifts at the edge of the beam cross-sections. When taking the difference ΔI between the two illuminations, these shifts produce a narrow but strong edge signal proportional to the radial tilt. The general wavefront reconstruction method consists of computing the wavefront surface from its Laplacian by solving a Poisson equation with the edge tilt as Neumann boundary conditions.

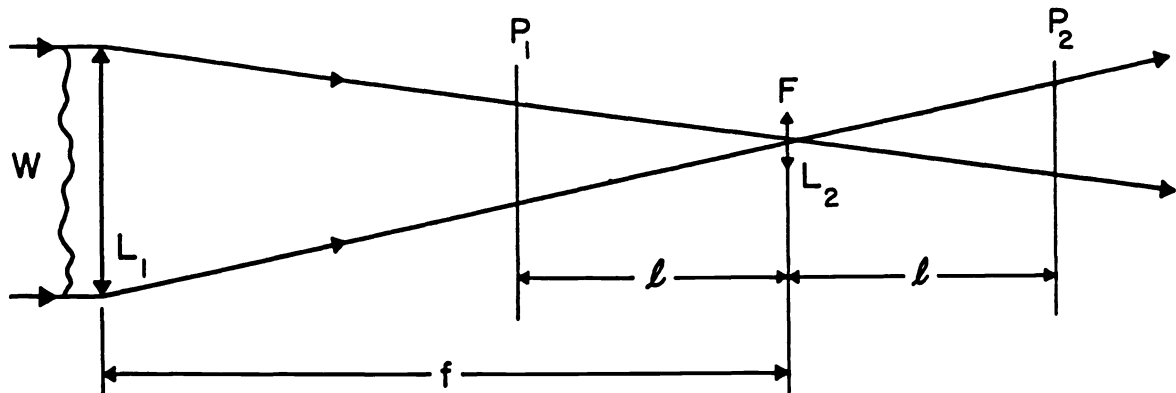


Fig. 1. The difference in illumination between planes P_1 and P_2 is a measure of the local curvature distribution in the incoming wavefront. It also measures the wavefront radial tilts at the edge.

When one observes stellar sources, atmospheric turbulence produces random fluctuations of the illumination in the out-of-focus images. However, over a typical 10–30 sec. exposure, these fluctuations average out. Only the average illumination is recorded, the distribution of which reveals permanent wavefront aberrations produced by the telescope optics. Physically, wavefront fluctuations diffract light over an angle α (the seeing disk size) so that the illumination in plane P_1 can be considered as a blurred pupil image with a blur size $\alpha(f - l) \approx \alpha f$. This blur must be small compared to the scale a of the wavefront corrugations we want to detect and measure. Since, in the image, they are scaled down by a factor l/f , the following condition has to be met:

$$\alpha f < \frac{a l}{f} \quad (2)$$

If $D = 2R$ is the diameter of the telescope objective, the maximum number of points in the reconstructed wavefront is

$$\frac{D}{a} = \frac{D l}{\alpha f^2} \quad (3)$$

Increasing l increases the number of points in the reconstructed wavefront but decreases ΔI , hence the sensitivity to small amplitude wavefront errors. When condition (2) is met, geometrical optics applies and Eq. (1) is valid.

3. EXPERIMENTAL DATA

On the night of April 17 to 18, 1989, the UH GEC CCD camera was installed at the UH 88-inch telescope prime focus, and after careful alignment, a series of out-of-focus images was recorded at different distances of the focal plane given by an encoder value. For each encoder value, four images were recorded. The encoder value (5965 minus raw reading) and the integration time of the processed images are given in Table 1. There are two sets of images: "A" images were taken inside focus; "B" images outside focus. Best focus was observed at encoder value 1500. At the primary focus, one encoder unit measures $12.7 \mu\text{m}$ and the f-ratio is 2.767. The CCD camera scale is $22 \mu\text{m}/\text{pixel}$. Magnitude 7–8 SAO stars were used close to zenith without any filter.

Figure 2 shows one of the A3 and B3 images as a typical example. These images were taken nearly at the same distance from the paraxial focus, on each side. The B3 image has been rotated by 180° for comparison with the A3 image. Most of the features seen on these images can also be seen in the other images. The most striking effect is the difference between the central obstruction ratio in the two sets of pictures. Images taken inside focus show an apparently smaller ratio and the illumination decreases toward the edge producing a so-called soft edge. The opposite effect is observed on images taken outside the focal plane. The central obstruction ratio is apparently larger and the illumination increases toward the edge producing a so-called sharp edge. These effects are characteristic of spherical aberration which is expected from images taken at an uncorrected Ritchey-Chretien prime focus.

Spherical aberration is described by a fourth order polynomial. Hence its second order derivative, the wavefront curvature is described by a second order polynomial. As a consequence, the difference between the illuminations observed on each side of the focal plane, which is a measure of the wavefront curvature, is expected to increase quadratically from the center to the edge. This is clearly seen in Fig. 3 which displays photometric profiles along a cross-section of the two images shown in Fig. 2. This strong aberration produces a huge difference between the inside focus and outside focus images which forbids the use of Eq. (1) to reconstruct the wavefront. Taking images further away from the focal plane would reduce the difference at the expense of a great loss in sensitivity to other aberrations.

This situation often occurs in optical testing for instance when testing a telescope mirror at the center of curvature. The standard approach

Table 1
List of Processed Images

Images	Encoder Value	Integration Time
A0	0	30.0 s
A1	300	20.0
A2	600	15.0
A3	750	20.0
A4	900	8.0
A5	1000	12.0
A6	1200	2.5
B5	1800	1.5
B4	2000	10.0
B3	2100	15.0
B2	2250	20.0
B1	2400	15.0
B0	2700	20.0
B00	3000	30.0

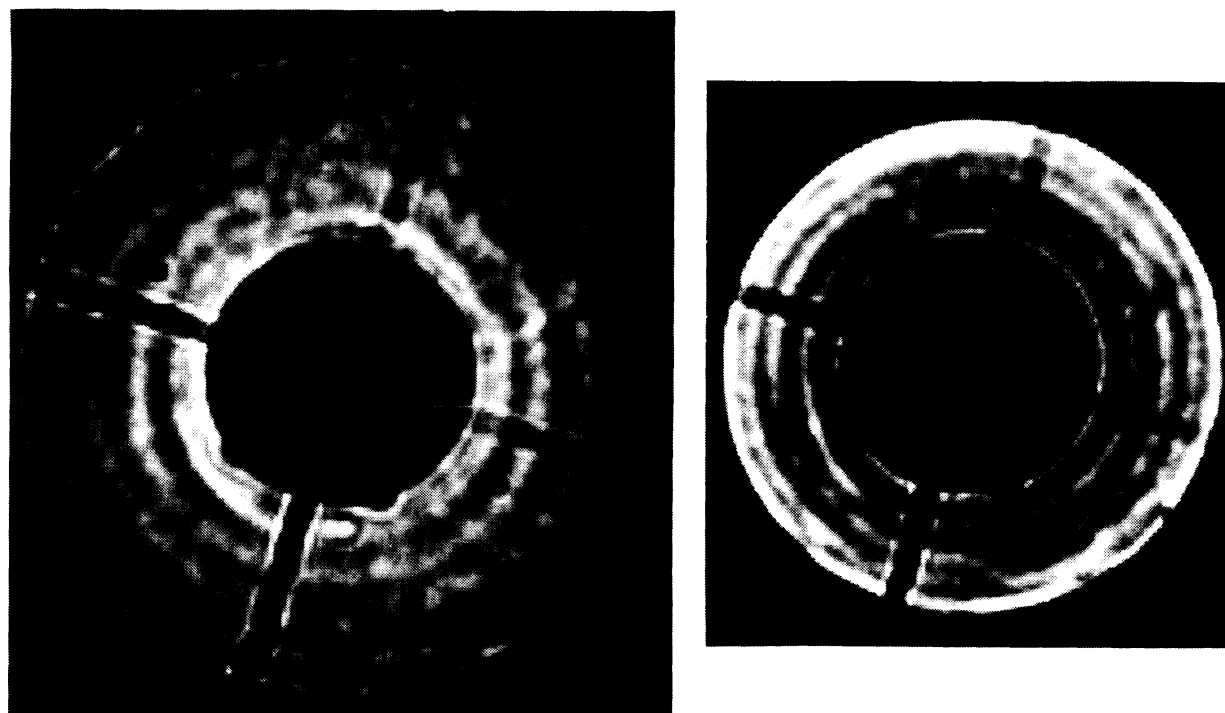


Fig. 2. Examples of images prior to correction. Left: inside focus A3 image. Right: outside focus B3 image.

consists of using a "null" lens to compensate the effect of spherical aberration. Here we have corrected the effect numerically. By the same token, one must also remove numerically the possibly large defocus term that would appear because the two images were recorded at positions that were not exactly symmetric about the paraxial focus, and any tilt term due to centroiding errors. The following sections describe how these aberration terms were estimated and removed.

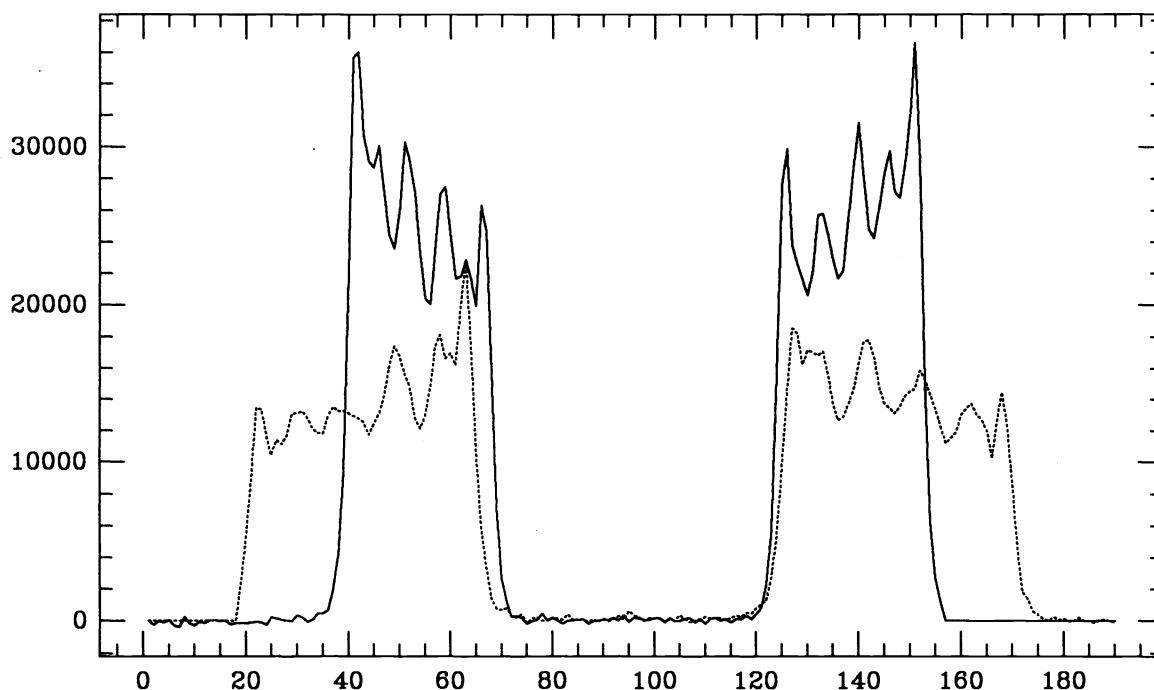


Fig. 3. Photometric profiles taken along a centered horizontal cross-section of the two images displayed in Fig. 2.

4. FIRST ESTIMATE OF THE ABERRATION TERMS TO BE REMOVED

We were able to estimate the spherical aberration and the position of the paraxial focus by tracing azimuthally-averaged marginal rays at the inner and outer edge of the pupil, using all of our images. The edges of the pupil were arbitrarily located where the illumination dropped to one sixtieth of that in the illuminated zone. The projections of the straight lines fitted to points inside focus do not exactly coincide with the straight lines fitted to points outside focus. The distance between the two lines was found to be of the order of two CCD pixels or 1.4 arcsecond and corresponds to the seeing disk diameter at one-sixth of the maximum (the FWHM value would, of course, be smaller). The plot of these rays shows the circle of least confusion to be located near encoder value 1500, as was originally estimated during the observations. The foci of the inner and outer marginal rays are found to be 90 encoder values apart. Let ΔZ_1 and ΔZ_2 be respectively the distances of the inner rays and outer rays foci to the paraxial focus. It can be shown⁶ that

$$\frac{\Delta Z_1}{\Delta Z_2} = \left(\frac{Y_1}{Y_2} \right)^2 \quad (4)$$

with $Y_1 = 0.37R$ for the inner edge of the pupil and $Y_2 = R$ for the outer edge.

The distance between the two foci is

$$\Delta Z_2 - \Delta Z_1 = \left[1 - \left(\frac{Y_1}{Y_2} \right)^2 \right] \Delta Z_1 = 0.86 \Delta Z_2 \quad (5)$$

Taking this distance as being 90 encoder values gives the longitudinal spherical aberration $\Delta Z_2 = 90/0.86 = 105$ encoder values or $1330 \mu\text{m}$. The transverse aberration ΔY_2 is obtained by dividing ΔZ_2 by twice the f ratio which gives $1330 / (2 \times 2.767) = 240 \mu\text{m}$. With these values, we calculate the Seidel aberration coefficient $A'_{040} = -10.9 \mu\text{m}$. The encoder value for the position of the paraxial focus is found to be 1425.

5. REMOVAL OF THE ABERRATION TERMS

In the out-of-focus images, aberrations translate into a geometrical transformation. Wavefront tilts translate into a lateral shift. Defocus translates into an expansion of the image so that a point with coordinates \vec{r} will be moved to the point with coordinates

$$\vec{r}_1 = \alpha \vec{r} \quad (6)$$

Flux conservation requires that

$$2\pi r_1 I(r_1) dr_1 = 2\pi r I(r) dr \quad (7)$$

where $r = |\vec{r}|$. Hence the new illumination $I(r_1)$ is

$$I(r_1) = \frac{1}{\alpha^2} I(r) \quad (8)$$

Spherical aberration translates into the following geometrical transformation⁷:

$$\vec{r}_2 = \vec{r}_1 + \beta r_1^2 \vec{r}_1 \quad (9)$$

Since

$$2\pi r_2 I(r_2) dr_2 = 2\pi r_1 I(r_1) dr_1 \quad (10)$$

the new illumination $I(r_2)$ is

$$I(r_2) = \frac{r_1}{r_2} \frac{1}{(1 + 3\beta r_1^2)} I(r_1) = \frac{1}{\alpha^2} \frac{r_1}{r_2} \frac{1}{(1 + 3\beta r_1^2)} I(r) \quad (11)$$

First we had to refine our estimation of the paraxial focus position and of the spherical aberration coefficient. In order to do that we took one A3 and one B3 image (the ones shown in Fig. 2), estimated the position of their centers to within a few tenths of a pixel, and then corrected them from the estimated defocus and spherical aberration. Knowing $I(r_2)$, one has to calculate $I(r)$. Since we are using our estimated center as the origin of the coordinate system, in general the sample points will not have integer coordinates. We proceed by first selecting a vector \vec{r} with integer coordinates (i, j) , and we calculate the coordinates of vector \vec{r}_2 as given by Eq. (9). The value of the illumination $I(\vec{r}_2)$ at point \vec{r}_2 is interpolated as a weighted sum of the illuminations observed at the four neighboring points. Weights are taken as the inverse of the point distances. The value of the new illumination at point $\vec{r}(i, j)$ is

$$I(\vec{r}) = \alpha^2 (1 + 3\beta r_1^2) \frac{r_2}{r_1} I(\vec{r}_2) \quad (12)$$

All the transformations are done at once to minimize errors due to interpolation. Once the transformations made on the two images, the illuminations are subtracted. The difference is divided by the mean image illumination and the wavefront is reconstructed by solving the Poisson equation as described in §2. Zernike terms are fitted to the reconstructed wavefront and residual values for the defocus and the spherical aberration are used to refine our above first estimate.

Our image transformations depend upon the two parameters α and β . The first parameter, α , depends only upon the estimated paraxial focus position. The second parameter, β , depends upon both the estimated focus position and the estimated spherical aberration coefficient. We have tested the influence of these estimated parameters on the reconstructed wavefront by taking a single pair of images and checking how sensitive our refined estimates of focal position and spherical aberration are to variations in the input estimates. We find the results to be quite robust.

6. ESTIMATION OF THE MIRROR CONIC CONSTANT

First we used our Poisson algorithm to reconstruct wavefronts from single pairs of appropriately transformed images. In each case the residual defocus and spherical aberration was estimated. This was done over a large number of image pairs. The average paraxial focus position was found to be 1430 encoder values with a r.m.s. dispersion of ± 2 or $25 \mu\text{m}$. The average value of the total Seidel aberration coefficient was found to be $-11 \pm 0.2 \mu\text{m}$. This value slightly exceeds the value $-10.2 \mu\text{m}$ expected from manufacturer's data. From now on we took 1430 as the encoder value for the paraxial focus. Transformations were made assuming either $-11 \mu\text{m}$ or the manufacturer's value $-10.2 \mu\text{m}$ for the Seidel aberration coefficient.

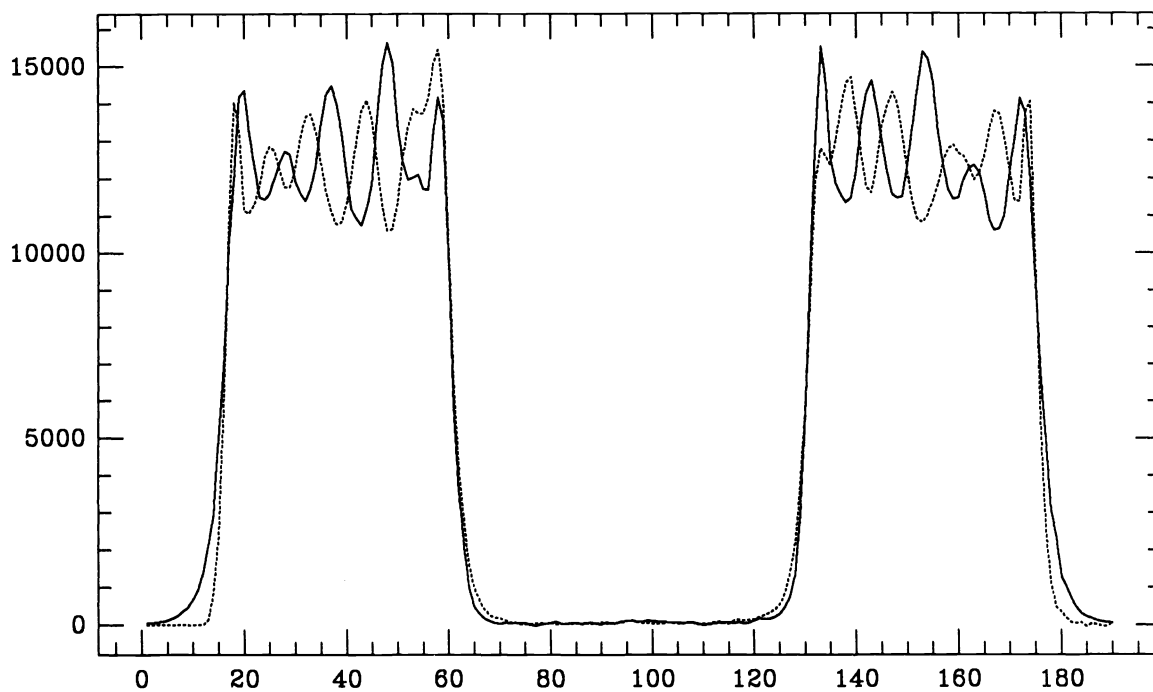


Fig. 4. Average profile of the transformed images. Solid line: B3; dotted line: A3.

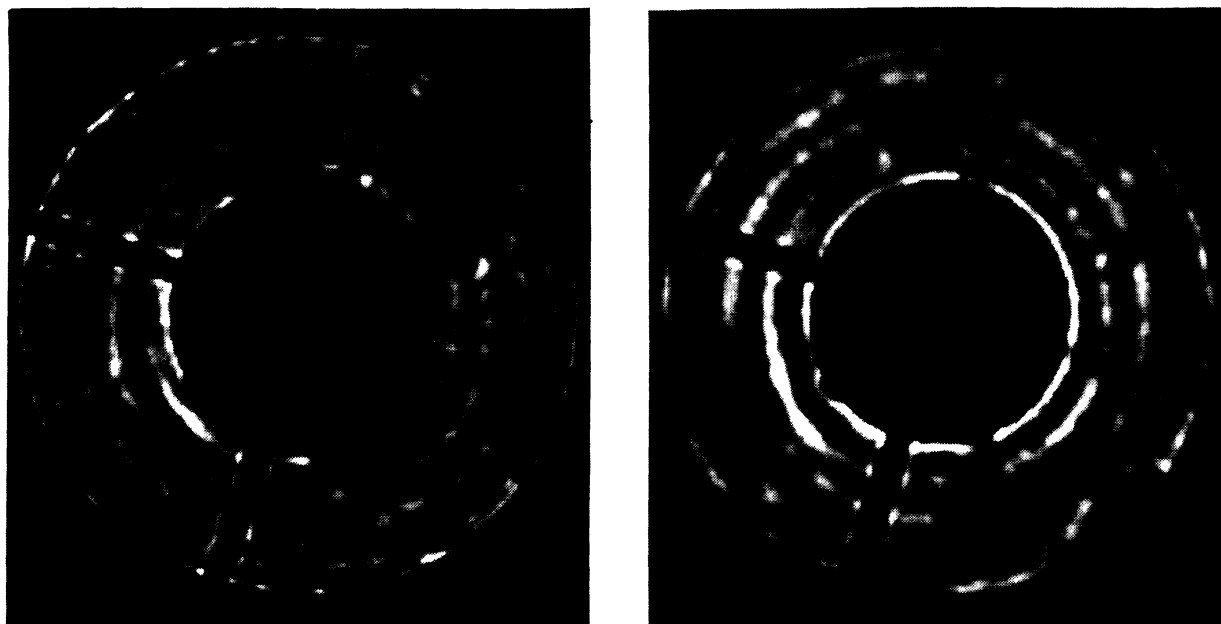


Fig. 5. Average transformed images. Left: A3; right: B3.

Among all the images, we selected pairs that were located as symmetrically as possible about the paraxial focus. The pairs A2—B2 and A3—B3 are the most symmetrically placed and were taken at a convenient distance from focus. Images A4 and B4, taken closer to focus, require stronger corrections. Images A1 have no associated images. We used both B0 and B1 images, which lie on either side of the desired focal distance and averaged the result. The results of the analysis of these images are summarized in Table 2. Our best estimate for the total Seidel spherical aberration coefficient at the telescope prime focus is

$$A'_{040} = -11 \pm 0.1 \mu\text{m}$$

For our mirror diameter and focal length, this value yields the following range for the mirror conic constant

$$-1.053 < \chi < -1.054$$

instead of the manufacturer's stated value $\chi = -1.04969$.

Table 2
Summary of Spherical Aberration Estimates

Number of independent images	Image sets	Initial Seidel aberration estimate (μm)	Total Seidel aberration (μm)
12	(A1, B0, B1)	-11.0	-10.99
16	(A2, B2), (A3, B3)	-10.2	-11.03
16	(A2, B2), (A3, B3)	-11.0	-11.02
8	(A4, B4)	-11.0	-10.94

7. RECONSTRUCTING THE MIRROR FIGURE

We now describe each step of the wavefront reconstruction process. We take the sets of A3 and B3 images as an example. The effect of image transformation can be seen in Fig. 4, which shows the average of the four images obtained at the B3 position (solid line), together with the average of the four image profiles obtained at the associated A3 position (dotted line). These transformed profiles can be compared with the original profiles shown in Fig. 3. Edge brightening and darkening have disappeared, and the two average images are now well matched. Moreover the irradiance fluctuations now coincide and are anticorrelated. This effect can be seen in more detail in Fig. 5, which displays the two average transformed images. Dark structures in one image appear as bright structures in the other and vice-versa. These structures are clearly produced by mirror figure errors.

Figure 6 shows a central horizontal cross-section of the sum of the two average images displayed in Fig. 5. Note the comparative uniformity. Values outside the illuminated area were replaced by the average illumination value and the result was smoothed over a 10 by 10 pixel window. The result (divided by two) is shown as a dotted line in Fig. 6 and was used to normalize the difference of the two images. The average B3 image was subtracted from the average A3 image. Figure 7 is a display of the normalized difference $\delta I/I$, the background gray level being zero. Dark structures are negative, bright structures are positive. This two-dimensional array is used as an input to our wavefront reconstruction algorithm.

As explained in §2, our wavefront reconstruction algorithm solves a Poisson equation in which the input signal is taken as the wavefront Laplacian all over the pupil area except within a thin annulus at the outer edge where the signal is taken as a measure of the wavefront radial edge slope. No boundary condition was given at the inner edge. As a consequence the algorithm interpolates the wavefront with a zero curvature surface inside the central obstruction. This part of the reconstructed wavefront was removed. The thickness of the outer edge annulus is taken as a free parameter, which should be one resolution element in the reconstructed wavefront over which data are averaged. A minimum value is the estimated seeing disk, in our case 4×4 pixels. Experience showed that the result is fairly insensitive to the choice of this parameter in a range extending from 4×4 to 8×8 pixels. The results presented here were obtained by taking averages over 6×6 pixels. The wavefront was reconstructed with 42 pixels across a pupil diameter. A fast iterative SOR

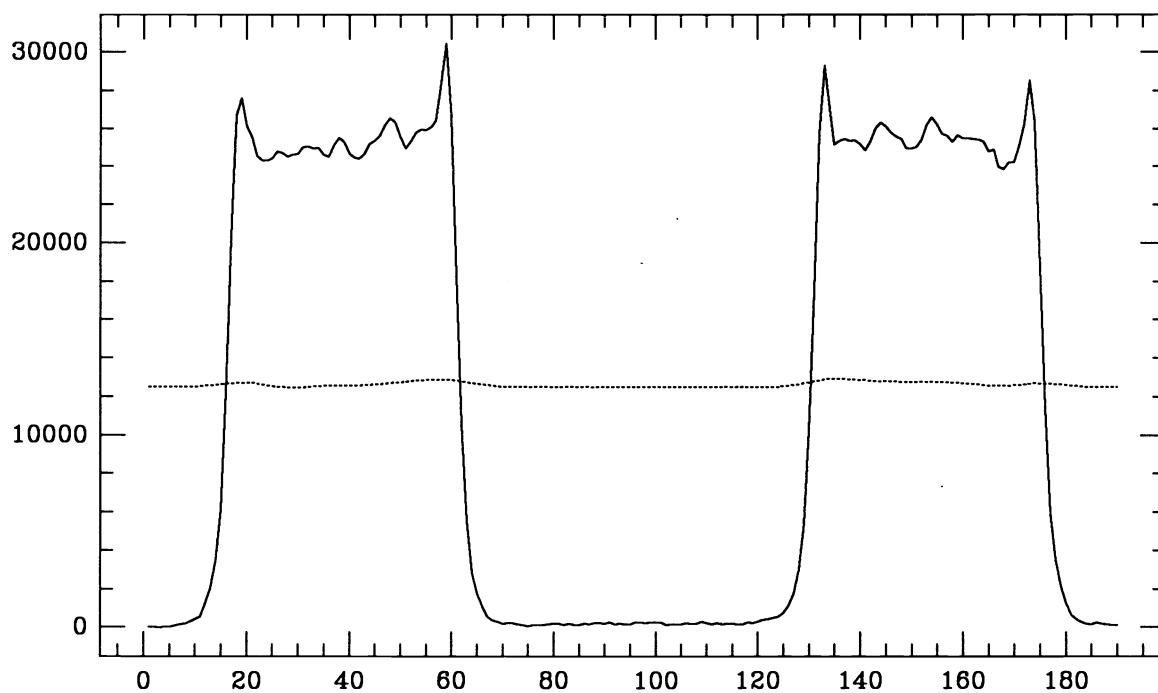


Fig. 6. Profile of the sum of the average transformed images. Dotted line: smoothed mean value.

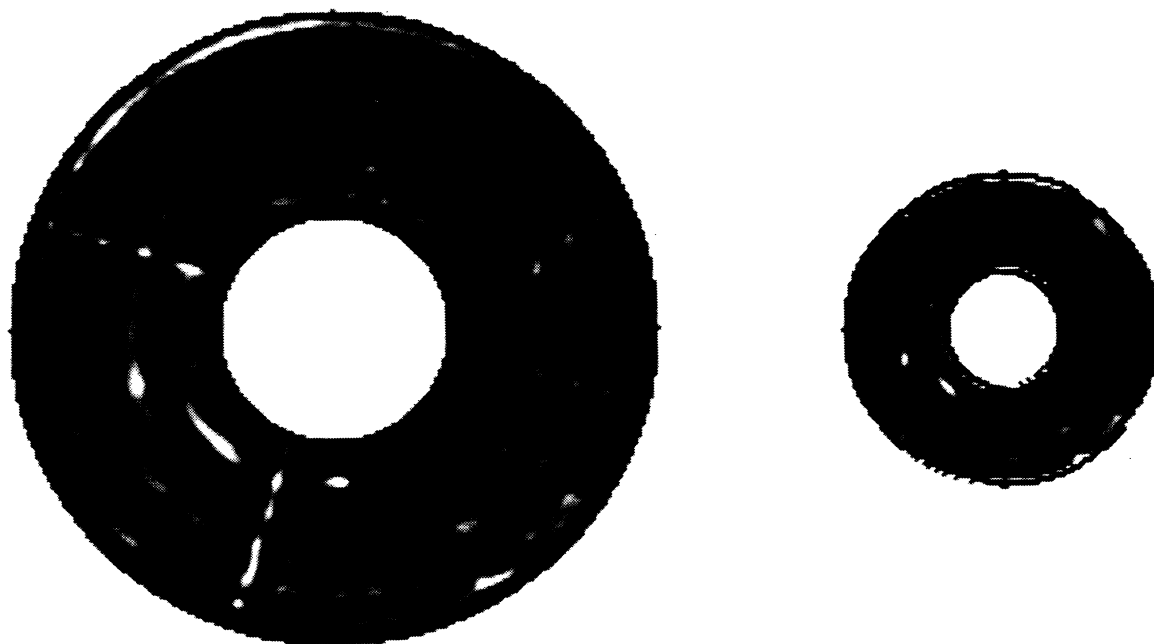


Fig. 7. Left: normalized difference between the two average transformed images. Right: Laplacian of the reconstructed wavefront shown for comparison. Gray background level is zero, dark is positive, and bright is negative.

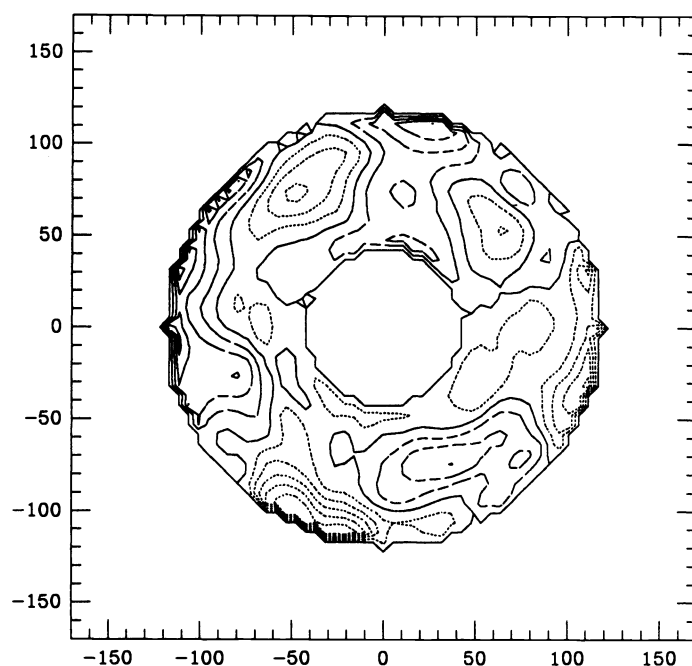


Fig. 8. Contour plot of the reconstructed mirror figure. Increment is $0.025\mu\text{m}$. Dotted line is positive, dashed line is negative.

algorithm is used to solve the Poisson equation⁸. Typical computation time is of the order of one minute on a Sun 4/280 computer.

A wavefront was reconstructed using each of the averaged image pairs indicated in Table 2. Zernike polynomials were fitted to the reconstructed wavefront and their coefficients estimated. Results were found to be fairly close. The highest dispersion was observed for coma and astigmatism. The uncertainty on astigmatism can be explained by the fact its Laplacian is zero. Hence the estimation is entirely obtained from the edge signal. We found a rather large astigmatism:

$$A_5 = 0.15 \pm 0.05\mu\text{m}$$

$$A_6 = 0.25 \pm 0.05\mu\text{m}$$

This is larger than the manufacturer's estimate of the mirror figure errors ($0.1\mu\text{m}$ on the wavefront), and is probably due to mirror support problems. This point deserves further investigation. Different results obtained for coma are easily explained by the fact that the images were taken at slightly different field positions.

Tilt, defocus, coma, astigmatism and any remaining spherical aberration were removed from the reconstructed wavefronts to obtain an estimate of the proper mirror figure. The resulting wavefronts were found to be almost identical. We averaged all of them. Hence the result presented here is based on a total of 52 independent images. Figure 8 shows a contour plot of the derived mirror figure. Wavefront amplitudes have been divided by two, to describe deviations of the mirror surface from the perfect shape. The increment is $0.025\mu\text{m}$. The root mean square deviation is found to be $0.04\mu\text{m}$ which is consistent with the manufacturer's claim of a $\lambda/10$ mirror surface accuracy. The largest deviations occur at the outer edge and seem to coincide in position and shape with mirror blank imperfections which can be seen clearly on a photograph of the blank we have examined. The maximum deviation is $\lambda/4$ at visible wavelengths.

The highest spatial resolution is obtained with the largest images. However images A1, B0, and B1 suffer from some uncertainty due to removal of a significant sky background. Hence we used images A2 and B2 to reconstruct the mirror figure with a slightly enhanced resolution. There are 78 pixels across a mirror diameter, with a physical pixel size of 2.8cm . Although, because of error propagation, a larger uncertainty is expected in this result, the estimated Zernike coefficients were found to be quite consistent with our previous results. The Zernike coefficients for astigmatism were found to be respectively $0.15\mu\text{m}$ and $0.27\mu\text{m}$.

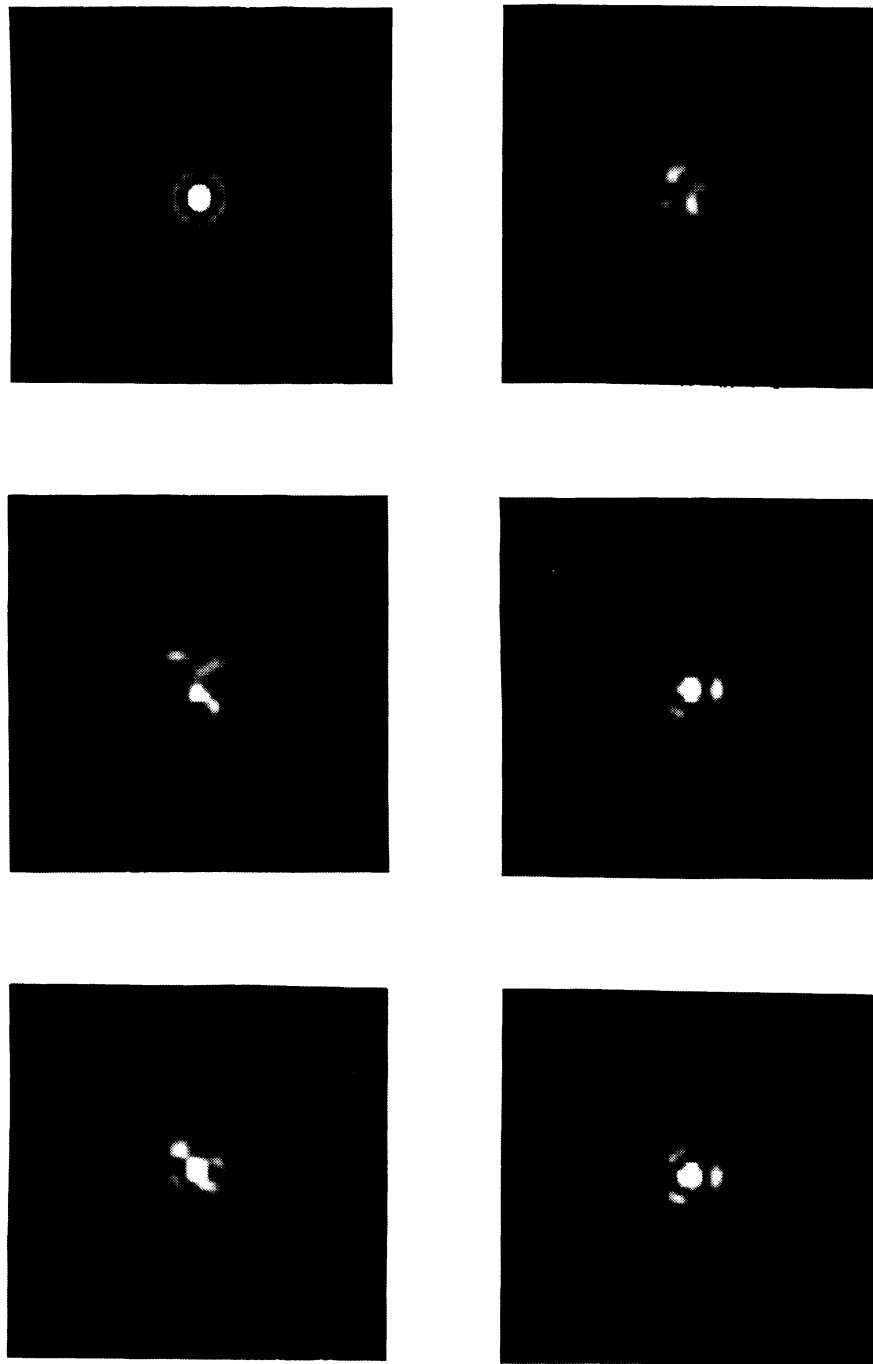


Fig. 9. From left to right and top to bottom: computed images *a*) diffraction-limited, $0.5\mu\text{m}$; *b*) with both astigmatism and residual spherical aberration, $0.5\mu\text{m}$; *c*) with astigmatism only, $0.5\mu\text{m}$; *d*) with neither astigmatism nor spherical aberration, $0.5\mu\text{m}$; *e*) same as *d*, $1\mu\text{m}$; *f*) same as *d*, $1.6\mu\text{m}$.

8. EFFECT OF ABERRATIONS ON IMAGE QUALITY

For each reconstructed wavefront one can compute the image it would produce by taking the squared modulus of the Fourier transform of the wavefront complex amplitude

$$\Psi(\vec{r}) = \exp \left[i \frac{2\pi Z(\vec{r})}{\lambda} \right] \quad (13)$$

where $Z(\vec{r})$ is the wavefront surface. The angular size in radian of one pixel in the Fourier transform is

$$1\text{pixel} = \frac{\lambda}{D} \times \frac{\text{number of pixels in pupil diameter}}{\text{number of points in the Fourier transform}} \quad (14)$$

In the following results, the scale has been converted into arc-seconds.

Images were calculated at four different wavelengths $\lambda = 0.5, 1.0, 1.6$, and $2.2\mu\text{m}$, using the average wavefront obtained from the A 2, A 3, B 2, and B 3 images, first after removal of tilt, defocus, coma, spherical aberration and astigmatism, then including the effect of astigmatism alone, and finally including the effect of both astigmatism and the excess of spherical aberration over the manufacturer's value, which is not supposed to be corrected by the present secondary mirror. Figures 9a–d display the images obtained at $\lambda = 0.5\mu\text{m}$. Figure 9a shows the diffraction-limited image. Figure 9d shows the image produced by the estimated mirror figure when the aberrations listed above are removed. Figure 9c includes the effect of astigmatism, and Fig. 9b includes the effects of both astigmatism and spherical aberration. A striking feature in Fig. 9d is the reinforcement of the first Airy ring at three points. This clearly suggests a deformation of the mirror on its main fixed three points support. Hence, if the mirror were properly supported, the mirror figure could be even better than what we estimated and displayed in Fig. 8. Figures 9e and f show images computed at $\lambda = 1\mu\text{m}$ and at $\lambda = 1.6\mu\text{m}$ without astigmatism or spherical aberration.

9. CONCLUSION

Analysis of extrafocal images appears to be a powerful tool to study the aberrations of optical telescopes. By analysing 52 images taken close to the prime focus of the 88-inch UH Ritchey-Chrétien telescope, we have been able to estimate the mirror conical constant with a one per thousand accuracy. Despite the large spherical aberration produced by the hyperbolic mirror at the prime focus, we have been able to estimate other aberrations with a good accuracy and to reconstruct the mirror figure with a high spatial resolution (3 cm resolved elements). The effect of the aberrations on the image has been studied.

The optical quality of the mirror appears to be excellent, but the conical constant differs significantly from the manufacturer's value. Some improvement in the image can be expected if a new secondary mirror is made accordingly. The other largest aberrations seem to be produced by the mirror supports and therefore could also be probably improved.

10. REFERENCES

1. A. Behr, "A proposal for the alignment of large telescopes," *Astron. Astrophys.* **28**, 355-358 (1973).
2. E. Ruiz, S. Cuevas, R. Langerica, R. Enriquez, L. Gutiérrez, L. Salas, "Offset guider/alignment system for the 2.1 m UNAM telescope," *SPIE* **627**, 231-235 (1986).
3. J.M. Beckers, J.T. Williams, MMT Technical Memorandum 79-1, Oct. 1979.
4. F. Roddier, "Curvature sensing and compensation a new concept in adaptive optics," *Appl. Opt.* **27**, 1223-1225 (1988).
5. F. Roddier, C. Roddier, N. Roddier, "Curvature sensing: a new wavefront sensing method," *SPIE* **976**, 203-209 (1988).
6. C. Roddier, A. Pickles, F. Roddier, A. Stockton, N. Roddier, "Report on the UH 88" Telescope Primary Mirror Figure," Institute for Astronomy Technical Report, Dec. 1989.
7. M. Born and E. Wolf, *Principles of Optics*, Macmillan, New York, 1964.
8. N. Roddier, "Curvature sensing and compensation for adaptive optics: a computer simulation," Master's thesis, Department of Electrical Engineering, University of Arizona (1989).